

# Ultracold Feshbach molecules in an orbital optical lattice

Received: 6 October 2022

Accepted: 10 February 2023

Published online: 20 March 2023

Yann Kiefer<sup>1,2</sup>, Max Hachmann<sup>1,2</sup> & Andreas Hemmerich<sup>1,2</sup>✉

Quantum gas systems provide a unique experimental platform to study the crossover between Bose–Einstein condensed molecular pairs and Bardeen–Cooper–Schrieffer superfluidity. The few studies in optical lattices have so far focused on the case when only the lowest Bloch band is populated, thus excluding orbital degrees of freedom. Here we demonstrate the preparation of ultracold Feshbach molecules of fermionic atoms in the second Bloch band of an optical square lattice. We cover a wide range of interaction strengths, including the regime of unitarity in the middle of the crossover. Binding energies and band relaxation dynamics are measured by means of a method resembling mass spectrometry. We find that the longest lifetimes arise for strongly interacting Feshbach molecules at the onset of unitarity. In the case of strong confinement in a deep lattice potential, we observe bound dimers also for negative values of the scattering length, extending previous findings for molecules in the lowest band.

The crossover between the regimes of Bose–Einstein condensation (BEC) and Bardeen–Cooper–Schrieffer (BCS) superfluidity is a hallmark of quantum gas physics<sup>1–8</sup>. Most studies work with nearly harmonic optical traps. BEC–BCS crossover physics in optical lattices<sup>9,10</sup> has been much less explored, and this research is limited to the lowest Bloch band, which exclusively provides local *s* orbitals. For example, in the ground state of a three-dimensional optical lattice, binding energies of strongly interacting fermionic potassium pairs have been studied<sup>11</sup>. Signatures of coherence and superfluidity have been reported<sup>12</sup> for strongly interacting fermionic lithium pairs. In an earlier study with fermionic potassium, prepared in the transverse ground state of an array of effectively one-dimensional (1D) wave guides<sup>13</sup>, Feshbach dimers have been shown to exist even at negative scattering lengths owing to a confinement-induced scattering resonance<sup>14,15</sup>. Recently, *p*-wave interacting atomic pairs tightly confined in excited motional states of isolated microscopic traps have been investigated<sup>16</sup>. Similarly, as orbital degrees of freedom in electronic condensed matter, for example, in transition metal oxides<sup>17,18</sup>, can give rise to unconventional order, the combination of the conventional BEC–BCS scenario with orbital physics in higher Bloch bands holds the intriguing perspective to discover unexplored fundamental many-body phases, such as exotic forms of superfluidity<sup>19</sup>. Examples of chiral, nematic or topological superfluids have been experimentally demonstrated for bosonic atoms in the

second Bloch bands of square<sup>20,21</sup>, triangular<sup>22</sup> or hexagonal<sup>23</sup> optical lattices, respectively. Extending these scenarios to composite bosons composed of pairs of fermionic atoms would open up a new regime of unconventional BEC–BCS physics.

In a recent study<sup>24</sup>, we demonstrated non-interacting spin-polarized fermionic potassium (<sup>40</sup>K) atoms and weakly interacting spin mixtures in higher Bloch bands of an optical square lattice. The present study investigates the vastly different regime of strong interactions between spin-up and spin-down fermions accessed by tuning a Feshbach resonance. This allows us to prepare bosonic Feshbach dimers<sup>25</sup>, composed of fermionic <sup>40</sup>K atoms, in higher Bloch bands of an optical square lattice. We study shallow and deep lattices, where the dimers can tunnel or are confined in 1D channels. A method inspired by mass spectrometry is applied to discriminate atoms and dimers by separating them in a ballistic time-of-flight protocol (Methods). This leads to images of the Brillouin zone (BZ) structures of atoms and molecules in velocity space, which differ in size by their mass ratio. This is seen in Fig. 1a for a mixture of molecules and atoms populating the second Bloch band. The molecules appear in the small second BZ and the atoms in the large second BZ, forming a nested structure according to the sketch in Fig. 1b. Hence, atoms and molecules can be separately counted. Using this method, we present measurements of binding energies, dissociation dynamics and exceptionally long

<sup>1</sup>Institut für Laserphysik, Universität Hamburg, Hamburg, Germany. <sup>2</sup>Zentrum für Optische Quantentechnologien, Universität Hamburg, Hamburg, Germany. ✉e-mail: [hemmerich@physnet.uni-hamburg.de](mailto:hemmerich@physnet.uni-hamburg.de)

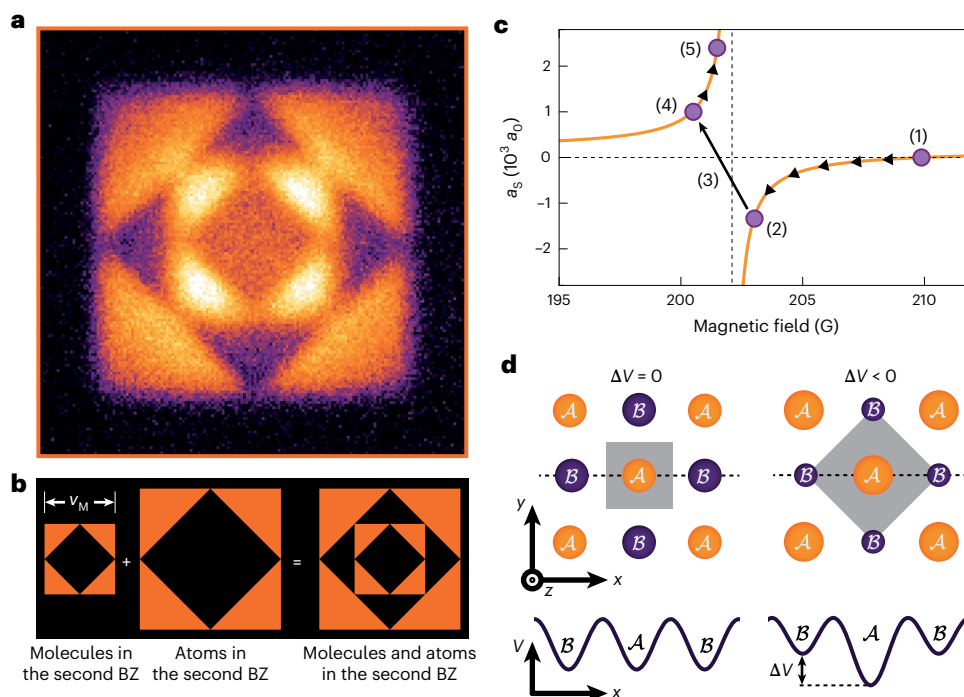


**Fig. 1 | Production and detection of Feshbach molecules.** **a**, A single mass spectrometry image of a mixture of  $^{40}\text{K}$  atoms and  $^{40}\text{K}$  Feshbach dimers excited to the second Bloch band. **b**, Composition of the image in **a** by the small second BZ of the molecules and the double-sized second BZ of the atoms. The velocity scale is  $v_M = \sqrt{2\hbar k/M}$  with  $k = 2\pi/\lambda$  and the mass  $M$  of the Feshbach dimers. **c**, Feshbach resonance and protocol for molecule preparation (see text).

The numbers (1)–(5) indicate successive steps in the experimental protocol. **d**, Sketch of the lattice geometry in the  $x$ – $y$  plane for  $\Delta V = 0$  (left) and  $\Delta V < 0$  (right). The grey shaded squares denote the corresponding Wigner–Seitz unit cells.  $\mathcal{A}$  and  $\mathcal{B}$  denote two classes of potential wells with tunable relative well depth. At the lower edge, sections along the dashed lines in the upper panels of **d** are shown.

molecule lifetimes for a wide range of interaction strengths including the strongly correlated regime. Such long lifetimes exceeding all other relevant timescales are crucial to study long-lived equilibrium states of the system.

## Production of ultracold Feshbach molecules

The production of Feshbach dimers in the second Bloch band of a square lattice proceeds as follows. A non-interacting spin-polarized degenerate Fermi gas of  $6 \times 10^5$  atoms of  $^{40}\text{K}$  in the state  $|F = 9/2, m_F = 9/2\rangle$  at a temperature of  $T = 0.17 T_F$  is prepared in an optical dipole trap, formed by two orthogonally intersecting laser beams with a wavelength of  $\lambda = 1,064$  nm, where  $T_F$  denotes the Fermi temperature. Here,  $F$  and  $m_F$  denote the total angular momentum and the magnetic quantum numbers, respectively. Note that for spin mixtures prepared at low magnetic fields, the lowest temperature reached in the optical dipole trap is  $T/T_F = 0.09$ . Next, a radio frequency with a constant value of 46 MHz is applied, while a homogeneous magnetic field  $B$  (pointing along the  $z$  axis) is ramped up from zero to approximately  $B_0 \approx 209.9$  G, such that a rapid adiabatic passage is obtained that inverts the sample to the  $|\downarrow\rangle \equiv |F = 9/2, m_F = -9/2\rangle$  state. Due to a Feshbach resonance located at  $B_{\text{res}} = 202.1$  G (ref. <sup>1</sup>), the  $s$ -wave scattering length for contact interaction between the states  $|\downarrow\rangle$  and  $|\uparrow\rangle \equiv |F = 9/2, m_F = -7/2\rangle$ , approximated as

$$a_s(B) = a_{\text{bg}}[1 - \Delta B/(B - B_{\text{res}})], \quad (1)$$

takes the value  $a_s(B_0) \approx 0$ , which corresponds to position (1) in Fig. 1c. Here,  $a_{\text{bg}} = 174 a_0$  is the background scattering length,  $a_0$  is the Bohr radius, and  $\Delta B = 7.8$  G is the width of the Feshbach resonance. Subsequently, the sample is adiabatically loaded into the lowest Bloch band of a bipartite optical square lattice, formed by two mutually orthogonal

standing waves with wavelengths  $\lambda = 1,064$  nm, oriented perpendicularly to the  $z$  axis (for details, see ref. <sup>24</sup>). The resulting optical potential is composed of two classes of independently tunable potential wells  $\mathcal{A}$  and  $\mathcal{B}$  arranged as the black and white squares of a checkerboard (Fig. 1d). In the  $x$ – $y$  plane, the lattice potential can be approximated by

$$V(x, y) = -V_0[\cos^2(kx) + \cos^2(ky)] - \frac{1}{2}\Delta V \cos(kx) \cos(ky) \quad (2)$$

with the wave number  $k = 2\pi/\lambda$ , the lattice depth parameter  $V_0$ , and  $\Delta V \equiv -4V_0 \cos(\theta)$  denoting the potential difference between the  $\mathcal{A}$  and  $\mathcal{B}$  wells. The experimental parameter  $\theta$  can be tuned within the interval  $[0, \pi]$ , that is,  $\Delta V \in 4V_0 \times [-1, 1]$ . Note that tightly bound dimers with mass  $M \equiv 2m$  possess twice the polarizability and hence twice the value of  $V_0$  as compared with atoms with mass  $m$ . Henceforth, we indicate lattice depth parameter values for atoms and molecules as  $V_0^{(m)}$  and  $V_0^{(M)} = 2V_0^{(m)}$ , respectively. Along the  $z$  direction, the atoms are held by the weak approximately harmonic confinement of the optical dipole trap, such that the lattice wells acquire a tubular shape. After lattice loading, we apply a radio-frequency pulse during 13  $\mu\text{s}$  to create a Fermi gas with equal populations in the states  $|\uparrow\rangle$  and  $|\downarrow\rangle$  at position (1) in Fig. 1c. Next, by tuning  $B$  to 202.3 G (compared with position (2) in Fig. 1c), the  $s$ -wave scattering length  $a_s$  for collisions between  $|\uparrow\rangle$  and  $|\downarrow\rangle$  is adjusted to a large negative value to obtain efficient evaporative cooling of the atomic sample in the presence of the lattice. Finally, the previously unpaired mixture of fermions is converted into bosonic molecules by adiabatically sweeping the magnetic field across the Feshbach resonance from 202.3 G to 200.46 G (indicated as step (3) in Fig. 1c). For the lowest temperatures, upon arrival at position (4) in Fig. 1c, we observe close to 100% conversion efficiencies with no

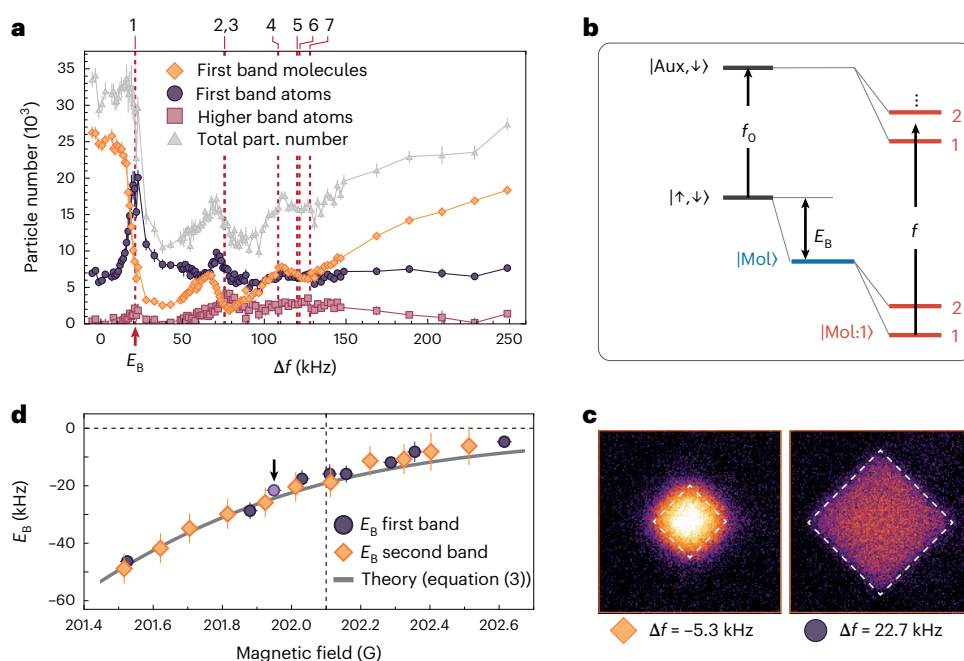


**Fig. 2 | Binding energies in a deep lattice. a**, A typical dissociation spectrum for a magnetic field  $B = 201.95$  G, that is, corresponding to the data point in **d** highlighted by an arrow, with molecules initially prepared in the lowest Bloch band ( $V_0^{(M)} = 40 E_{\text{rec}}^{(M)}$ ,  $\theta = 0.4\pi$ ). The orange diamonds and dark purple circles show the molecule and atom populations in the first band, respectively, plotted against  $\Delta f = f - f_0$ , with the irradiated radio frequency  $f$ , and  $f_0$  according to **b**. The leftmost vertical red dashed line indicates the frequency, where the first substantial drop of the molecule population and a corresponding peak of the atom population in the first band is observed. This frequency is identified with the molecular binding energy  $E_B$ . Further dashed vertical lines denote the positions of higher Bloch bands  $|\text{Aux}, \downarrow : \nu\rangle$  with  $\nu \in \{2, 3, 4, 5, 6, 7\}$ , leading to

further resonant molecule dissociation (compare **b**). The error bars show the standard deviation of the mean for 15 experimental runs. **b**, Diagram showing the relevant atomic and molecular energy levels and excitation frequencies. **c**, Mass spectrometry images for  $\Delta f = -5.3$  kHz (left) and  $\Delta f = 22.7$  kHz (right). The white dashed rectangles show the first BZ for molecules (left) and atoms (right). **d**, Measured binding energies for molecules prepared in the first (dark purple discs) and second (orange diamonds) Bloch band with ( $V_0^{(M)} = 40 E_{\text{rec}}^{(M)}$ ,  $\theta = 0.4\pi$ ) and ( $V_0^{(M)} = 60 E_{\text{rec}}^{(M)}$ ,  $\theta = 0.54\pi$ ), respectively. The error bars are estimated from the spectral width of the underlying dissociation resonance. The dashed vertical line indicates the position of Feshbach resonance  $B_{\text{res}}$ . The grey line shows a calculation using equation (3).

discernible atomic fraction. Next, a quench from an initial value  $\theta \approx 0.4\pi$ , used for loading the lowest band, to  $\theta \approx 0.53\pi$  efficiently prepares a large fraction of the atoms or molecules in the second band (for details, see ref. <sup>24</sup>). By means of a final adiabatic change of  $B$  (position (5) in Fig. 1c), we may subsequently tune to a desired target value of  $a_s$ , which lets us adjust the molecular binding energy.

## Binding energies

Binding energies of Feshbach molecules are measured by dissociating them with a 5 ms radio-frequency pulse, converting  $|\uparrow\rangle$  atoms into atoms in the auxiliary state  $|\text{Aux}\rangle \equiv |F = 9/2, m_F = -5/2\rangle$ . The unbound  $|\downarrow\rangle$  atoms, which remain trapped in the optical lattice, are readily discriminated from the molecules as explained in the context of Fig. 1a,b and in Methods.

Let us first discuss the case of a deep optical lattice, such that tunnelling is practically suppressed for molecules and their motion is restricted to quasi-1D tubes along the  $z$  direction. An example for this regime is realized by adjusting  $V_0^{(M)} = 40 E_{\text{rec}}^{(M)}$ ,  $\theta = 0.4\pi$  and hence  $\Delta V^{(M)} = -49.4 E_{\text{rec}}^{(M)}$  with  $E_{\text{rec}}^{(M)} \equiv \frac{\hbar^2 k^2}{2M}$  denoting the single-photon recoil energy for molecules, where  $\hbar$  denotes the reduced Planck constant. A typical example of a dissociation spectrum for molecules  $|\text{Mol} : 1\rangle$  prepared in the lowest band is shown in Fig. 2a for  $B = 201.95$  G corresponding to the data point in Fig. 2d indicated by an arrow. We plot the numbers of molecules (diamonds) and atoms (circles) in the lowest band, the atoms in all excited bands (squares), and the total number of particles, that is, atoms plus molecules (triangles), against  $\Delta f = f - f_0$ , that is, the applied radio frequency  $f$  minus the  $|\uparrow\rangle \rightarrow |\text{Aux}\rangle$  transition frequency  $f_0$  (Fig. 2b). The latter depends only on  $B$  and is readily

measured after preparing a pure  $|\uparrow\rangle$  sample in the dipole trap. Hence,  $\Delta f = 0$  corresponds to zero molecular binding energy.

To understand the spectral features in Fig. 2a, it helps to first look at the atomic and molecular levels sketched in Fig. 2b. The black horizontal bars show the energies of the bare two-atom states  $|\uparrow, \downarrow\rangle$  and  $|\text{Aux}, \downarrow\rangle$  separated by the frequency  $f_0$ . The blue horizontal bar shows the energy of the Feshbach molecules  $|\text{Mol}\rangle$  made of atom pairs  $|\uparrow, \downarrow\rangle$ , shifted by the binding energy  $E_B$ . The red horizontal bars show the additional energy shifts for the Bloch bands due to the presence of the optical lattice. The molecules  $|\text{Mol}\rangle$  are prepared in the lowest molecular band, denoted  $|\text{Mol} : 1\rangle$  in Fig. 2b. As the radio frequency  $f$  is increased, we expect the first drop of the molecular population in  $|\text{Mol} : 1\rangle$ , when  $f$  reaches the resonance frequency  $f_i$  for the transition  $|\text{Mol} : 1\rangle \rightarrow |\text{Aux}, \downarrow : 1\rangle$  such that unbound atoms in the first Bloch band are produced. According to Fig. 2a, this occurs at  $\Delta f = \Delta f_i \equiv 22.7$  kHz, which is identified with the value of the binding energy  $E_B$ . To further illustrate the conversion of molecules into atoms, mass spectrometry images are shown in Fig. 2c for  $\Delta f = -5.3$  kHz, well below  $\Delta f_i$  (left), and at  $\Delta f = \Delta f_i$  (right). In fact, in Fig. 2c (left), predominantly molecules in the first BZ are seen, while in Fig. 2c (right), most molecules are dissociated into atoms, giving rise to a first BZ expanded by a factor of 2.

At larger values of  $\Delta f > \Delta f_i$ , further resonances occur, leading to reduced molecule numbers due to dissociation into higher bands  $|\text{Aux}, \downarrow : \nu\rangle$  with  $\nu \in \{2, 3, 5, 6, 7\}$ . The respective resonance frequencies are readily calculated by a band structure calculation and are plotted in Fig. 2a as vertical dashed red lines. Note that, for the fourth band  $\nu = 4$ , no resonance arises, which can be explained by the small Franck-Condon overlap between the wave function of  $|\text{Mol} : 1\rangle$  and  $|\text{Aux}, \downarrow : 4\rangle$ . This has been checked by calculating the respective Bloch functions,



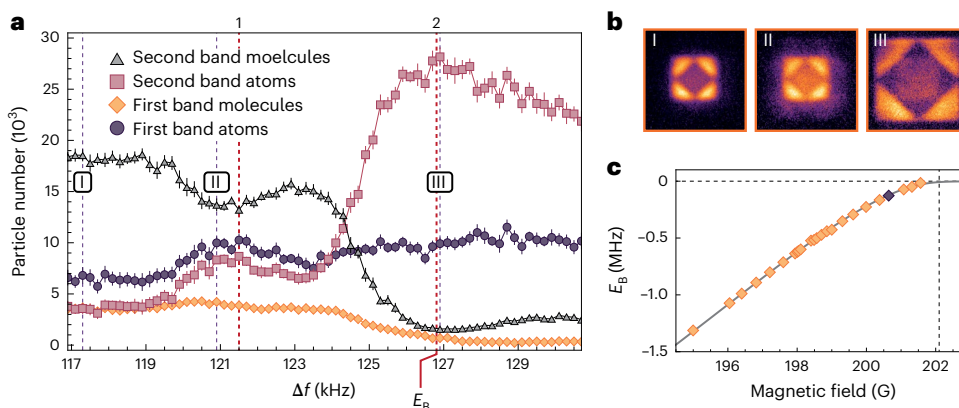


**Fig. 3 | Binding energies in a shallow lattice. a**, Dissociation spectrum for molecules initially prepared in the second band with a lattice depth parameter  $V_0^{(M)} = 10 E_{\text{rec}}^{(M)}$  and  $\theta = 0.54\pi$ . The magnetic field is  $B = 200.6$  G corresponding to the dark purple diamond in **c**. Orange diamonds (dark purple discs) show populations of molecules (atoms) in the first band. Grey triangles (magenta squares) show populations of molecules (atoms) in the second band. The red dashed lines indicate the two frequencies  $\Delta f_1$  and  $\Delta f_2$ , where dissociation maximally depletes the population of molecules in the second band. The error

bars show the standard deviation of the mean for 15 experimental runs. **b**, Mass spectrometry images for the values of  $\Delta f$  indicated by I, II and III in **a**. **c**, Binding energies (orange diamonds) of molecules in the second band obtained from spectra as plotted in **a** for varying magnetic fields. The errors are estimated from the spectral width of the underlying dissociation resonance to be less than 5 kHz, which is an order of magnitude smaller than the data symbols. The grey solid line presents the theoretical prediction of equation (3).

with the result that  $|\text{Mol} : 1\rangle$  predominantly resides in the deep wells and  $|\text{Aux}, \downarrow : 4\rangle$  in the shallow wells.

Dissociation spectra as in Fig. 2a let us determine the binding energies for molecules prepared in the first (dark purple circles) and second (orange diamonds) bands, shown in Fig. 2d. The grey solid line shows a calculation using the implicit equation

$$\frac{a_s - r_0}{(1 + \delta)a_r} = -\frac{1}{\zeta(1/2, -E_B/2\hbar\omega_r)}. \quad (3)$$

adapted from ref. <sup>15</sup> for a single 1D tubular potential, where  $\zeta$  denotes the Hurwitz zeta function. We insert the radial fundamental frequency  $\omega_r$ , measured in the radially symmetric quasi-1D tubes of our lattice, and the associated harmonic oscillator length  $a_r \equiv \sqrt{\hbar/\mu\omega_r}$  for the relative atomic motion with  $\mu$  denoting the reduced atomic mass. We multiply  $a_r$  by  $1 + \delta$  with a small positive  $0 < \delta \ll 1$ , to account for the anharmonicity of the tube potential. The free space s-wave scattering length  $a_s$  is expressed as a function of the magnetic field  $B$  according to equation (1). Finally, following ref. <sup>26</sup>, to account for a realistic van der Waals scattering potential  $-C_6/r^6$ , we introduce the finite range parameter  $r_0 = (mC_6/32\hbar^2)^{1/4} \Gamma(3/4)/\Gamma(5/4)$  and replace  $a_s$  by  $a_s - r_0$ . Here,  $r$  is the relative coordinate,  $C_6$  is a constant and  $\Gamma$  denotes the Gamma function. From refs. <sup>27,28</sup>, we take  $C_6 = 3,926a_0$  and  $r_0 = 65a_0$ . Note that equation (3) is configured such that for zero interaction, zero binding energy is obtained. This theoretical model, based on refs. <sup>14,15,26</sup>, reproduces the binding energies in Fig. 2d remarkably well if one sets  $\delta = 0.142$ , which reasonably well agrees with the expected anharmonicity. The model accounts for effects of reduced dimensionality arising if the degree of radial confinement becomes comparable with  $a_s$ , giving rise to a confinement-induced resonance of the effective 1D scattering cross-section. As a consequence, bound states become possible for negative values of  $a_s$  as is seen in Fig. 2d (see also ref. <sup>13</sup>). Note that Fig. 2d shows equal binding energies for molecules prepared in the first and second bands. This results from engineering the lattice potentials via adjustment of  $V_0$  and  $\Delta V$ , such that the lattice wells with predominant population, that is, the deep (shallow) wells, if the molecules are prepared in the first (second) band, exhibit equal values of  $\omega_r$  and  $a_r$ . For example, with  $V_0^{(M)} = 40 E_{\text{rec}}^{(M)}$  and  $\theta = 0.4\pi$  for molecules in the first band, and  $V_0^{(M)} = 60 E_{\text{rec}}^{(M)}$  and  $\theta = 0.54\pi$  for molecules in the second band, as used in Fig. 2d,  $\omega_r = 2\pi \times 30$  kHz is obtained.

Next, we discuss molecules prepared in the second band ( $|\text{Mol} : 2\rangle$ ) for a shallow lattice with  $V_0^{(M)} = 10 E_{\text{rec}}^{(M)}$ ,  $\theta = 0.54\pi$  and hence  $\Delta V^{(M)} = 5 E_{\text{rec}}^{(M)}$  for an extended range of the magnetic field below the Feshbach resonance,  $B < B_{\text{res}}$ . In Fig. 3a, we show a dissociation spectrum for molecules at  $B = 200.6$  G corresponding to the dark purple diamond-shaped data point in Fig. 3c. The plot in Fig. 3a shows the second band molecules (grey triangles), whose number is initially maximized, second band atoms (magenta squares), and molecules (orange diamonds) and atoms (dark purple circles) in the first band. The red dashed lines emphasize the frequencies  $\Delta f_1$  and  $\Delta f_2$ , where local minima in the number of molecules in the second band are found, due to maximal efficiency of the dissociation process. At frequencies  $\Delta f \ll \Delta f_1$ , dissociation is not resonant such that in mass spectrometry images, one observes the second BZ filled with molecules, as exemplified in I in Fig. 3b, recorded at position I in Fig. 3a. At the left red dashed line ( $\Delta f_1$ ), dissociation arises due to a transition, mainly exciting second band molecules  $|\text{Mol} : 2\rangle$  to atomic pairs  $|\text{Aux}, \downarrow : 1\rangle$  in the first band. This is confirmed by the mass spectrometry image in II in Fig. 3b, recorded at position II in Fig. 3a, close to the left red dashed line. Here, a partial filling of the first BZ with atoms is observed. The dissociation process shows limited efficiency due to the small Franck–Condon overlap between the wave functions involved, similarly as discussed in the context of Fig. 2a for the transition  $|\text{Mol} : 1\rangle \rightarrow |\text{Aux}, \downarrow : 4\rangle$ . Around the second red dashed line ( $\Delta f_2$ ), the dissociation transition couples  $|\text{Mol} : 2\rangle$  to  $|\text{Aux}, \downarrow : 2\rangle$ . Both states belong to second bands with a sizable Franck–Condon overlap, such that the dissociation around  $\Delta f_2$  is notably more efficient than for  $\Delta f_1$ , as seen by the nearly complete depletion of the molecule population in Fig. 3a around 127 kHz. III in Fig. 3b confirms that the dissociated atoms in fact arise in the second band, giving rise to a filled second BZ for atoms, twofold increased compared with the second BZ for molecules in I in Fig. 3b. Note that  $\Delta f_2 - \Delta f_1$  is approximately given by the separation of the second and first bands for atoms. A determination of  $\Delta f_1$ ,  $\Delta f_2$  below the scale of a few kilohertz is not supported by the width of the spectral features observed near the red dashed lines in Fig. 3a. In Fig. 3c, binding energies for molecules in the second band are shown, measured by analysing dissociation spectra as in Fig. 3a for different magnetic fields. The grey solid line represents the theoretical prediction according to equation (3), showing remarkable agreement.

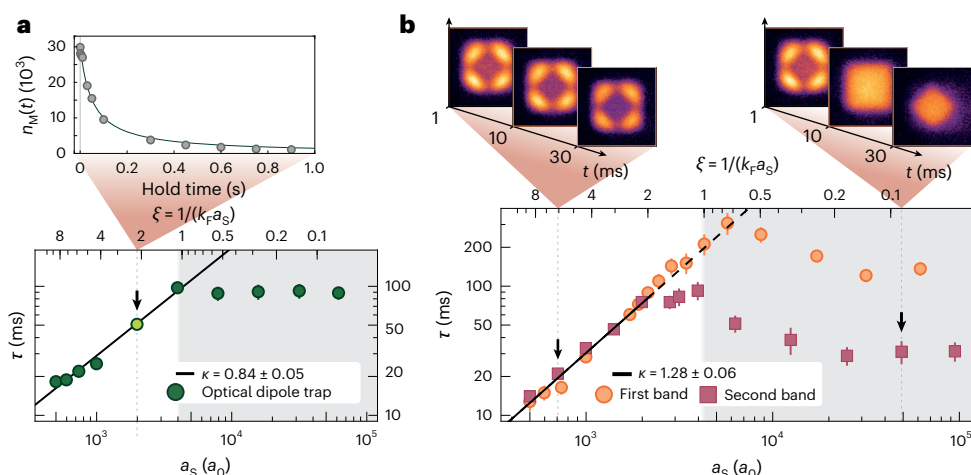


**Fig. 4 | Relaxation dynamics.** **a**, Half-lives  $\tau$  of Feshbach dimers in the dipole trap plotted versus  $\xi$  (upper axis) and  $a_s$  (lower axis). The inset shows an exemplary measurement of  $\tau$  for the light green data point indicated by the black arrow. The black solid line is a fit for the domain  $\xi > 2$  with a straight line, extrapolated to the domain  $\xi < 2$ , indicating a power law  $\tau \propto \xi^{-\kappa}$  with  $\kappa = 0.84 \pm 0.05$ . **b**, Half-lives of Feshbach dimers prepared in the first and second Bloch bands of an optical lattice (orange circles and magenta squares, respectively). The lattice depth is  $V_0^{(M)} = 8E_{\text{rec}}^{(M)}$  and  $\theta = 0.4\pi$  for the first Bloch band and  $0.535\pi$  for the second Bloch band. The black solid line is a common fit for data of both bands within the

domain  $\xi > 2$  with a straight line, extrapolated to the domain  $\xi < 2$  (dashed continuation), indicating a power law  $\tau \propto \xi^{-\kappa}$  with  $\kappa = 1.28 \pm 0.06$ . The error bars for  $\tau = (n_0\beta)^{-1}$  in **a** and **b** are determined by propagating the errors for  $n_0$  and  $\beta$  obtained in the fit procedure applied to determine  $\tau$ . For data symbols with no visible error bar, the error is smaller than the symbol diameter. Each data point in a lifetime measurement averages over six experimental repetitions. The insets at the top boundary of **b** illustrate the different relaxation paths found in the second Bloch band for small and large  $\xi$ .

## Molecular decay dynamics

In this section, we discuss the observation of two relaxation channels for Feshbach dimers<sup>29</sup>. The first process dominates for  $\xi \equiv (k_F a_s)^{-1} \gg 1$  ( $k_F$ , Fermi momentum), that is, for relatively weak scattering lengths, where Feshbach dimers become deeply bound. In this regime, the primary relaxation process is based on inelastic dimer–dimer collisions, where one molecule gains binding energy, while the other is dissociated, such that both molecules are lost. Dimer–atom collisions are less relevant as our experiments start with a nearly pure molecule sample. Larger binding energies provide larger Franck–Condon overlap between the involved molecular wave functions, so that the molecular lifetime  $\tau$  should decrease with  $\xi$ , in accordance with the scaling  $\tau \propto (a_s)^{2.55}$  predicted in absence of a lattice<sup>30</sup>. In the other extreme for  $\xi \ll 1$ , according to ref.<sup>30</sup>, the elastic dimer–dimer scattering length  $a_{\text{dd}}$  scales as  $a_{\text{dd}} \approx 0.6a_s$ , and hence due to the large size of  $a_s$ , molecular three-body collisions are expected to introduce molecule loss and to give rise to a lifetime that decreases, when  $\xi$  approaches zero.

In Fig. 4a, we benchmark the lifetimes of the Feshbach molecules trapped in the approximately harmonic optical dipole trap. After the dimers are formed (Fig. 1c), the scattering length  $a_s$  is adjusted to a desired value via the magnetic field according to equation (1), and the dimers are held for a variable time in the trap. To count the remaining number of molecules  $n_M$ , the magnetic field is rapidly tuned to  $B_{\text{img}} = 200.46$  G, associated with a moderate value of  $a_s$ , and the molecules are allowed to ballistically expand (nearly unimpaired by interaction) during 22 ms, before an absorption image of the  $|\uparrow\rangle$  atoms is recorded. The dimer population plotted against the hold time is fitted with the two-body decay model  $\dot{n}_M = -\beta n_M^2$ , with the two-body collision parameter  $\beta$ , the solution  $n(t) = n_0 \times (1+t/\tau)^{-1}$ , the initial number of molecules  $n_0 \equiv n(0)$ , and the half-time of the molecule sample  $\tau \equiv (n_0\beta)^{-1}$ . An exponential fit, assuming density independent loss, or a three-body decay model fails to describe the data. The obtained half-time  $\tau$  is plotted in Fig. 4a versus  $\xi$  and  $a_s$ . The inset shows an exemplary measurement of  $\beta$  and  $n_0$  leading to the light green data point indicated by a black arrow. The main panel shows strikingly different behaviour in the unitarity regime  $\xi < 1$ , where a nearly

constant half-time  $\tau$  around 100 ms is observed, and in the regime  $\xi > 1$ , where the data are well fitted with a straight line, indicating a power law  $\tau \propto \xi^{-\kappa}$  with an exponent  $\kappa = 0.84 \pm 0.05$ . The largest values of  $\tau$  are found at  $\xi \approx 1$ . Note that  $\kappa$  does not agree with the predicted value of 2.55 for dimer–dimer collisions in ref.<sup>30</sup> or the experimental value of  $\sim 2.3$  for mixed dimer–dimer and dimer–atom collisions, reported in ref.<sup>2</sup>.

In Fig. 4b, an analogous analysis is carried out in presence of a shallow optical lattice with  $V_0^{(M)} = 8E_{\text{rec}}^{(M)}$ , which permits nearest-neighbour tunnelling on a submillisecond timescale. The orange circles show the observed half-lives for molecules prepared in the first Bloch band with  $\theta = 0.4\pi$  and hence  $\Delta V_0^{(M)} = -9.88E_{\text{rec}}^{(M)}$ . The magenta squares correspond to  $\theta = 0.535\pi$  (that is,  $\Delta V_0^{(M)} = 3.51E_{\text{rec}}^{(M)}$ ) for molecules prepared in the second Bloch band. In the regime  $\xi > 2$ , both datasets show the same dependence on  $\xi$  and are fitted with the same straight line (black solid line in Fig. 4b), indicating a power law model  $\tau \propto \xi^{-\kappa}$  with  $\kappa = 1.28 \pm 0.06$ . The dashed black line is a continuation into the  $\xi < 2$  domain. Note that also in the presence of a lattice,  $\kappa$  does not agree with the predicted value of 2.55 in ref.<sup>30</sup> or the experimental value of  $\sim 2.3$  from ref.<sup>2</sup>, both obtained for a scenario without a lattice. For  $\xi < 1$ , we find that  $\tau$  grows with increasing  $\xi$ . While the data for the second band very well agree with the results for the first band in the entire range  $\xi > 2$ , for  $\xi < 2$ , a dramatic decrease of  $\tau$  is observed for the second band, which only increases to a threefold shorter lifetime than observed for the first band. This indicates that an additional relaxation channel opens for the second band if  $\xi < 2$ . In fact, as illustrated in the two insets at the upper edge of Fig. 4b, for  $\xi$  close to zero, for example, for  $\xi \approx 0.1$ , we see an initial pronounced decay of molecules into the first band, followed by a subsequent decay of the first band population, while in the domain  $\xi > 2$ , for example, close to  $\xi \approx 6$ , the molecules do not initially transit to the first band during relaxation. This may be explained as follows. For small  $\xi$ , that is, large  $a_s$ , in the second band, the increasing elastic binary collision cross section can lead to a redistribution of energy from the lattice plane into the tube direction, which gives rise to an additional escape channel from the lattice (see also ref.<sup>31</sup>).

## Online content

Any methods, additional references, Nature Portfolio reporting summaries, source data, extended data, supplementary information, acknowledgements, peer review information; details of author contributions and competing interests; and statements of data and code availability are available at <https://doi.org/10.1038/s41567-023-01994-9>.

## References

- Regal, C. A., Greiner, M. & Jin, D. S. Observation of resonance condensation of fermionic atom pairs. *Phys. Rev. Lett.* **92**, 040403 (2004).
- Regal, C. A., Greiner, M. & Jin, D. S. Lifetime of molecule–atom mixtures near a Feshbach resonance in  $^{40}\text{K}$ . *Phys. Rev. Lett.* **92**, 083201 (2004).
- Zwierlein, M. W. et al. Condensation of pairs of fermionic atoms near a Feshbach resonance. *Phys. Rev. Lett.* **92**, 120403 (2004).
- Bourdel, T. et al. Experimental study of the BEC–BCS crossover region in lithium 6. *Phys. Rev. Lett.* **93**, 050401 (2004).
- Bartenstein, M. et al. Crossover from a molecular Bose–Einstein condensate to a degenerate Fermi gas. *Phys. Rev. Lett.* **92**, 120401 (2004).
- Ketterle, W. & Zwierlein, M. W. Making, probing and understanding ultracold Fermi gases. *Riv. del Nuovo Cim.* **31**, 247–422 (2008).
- Zwerger, W. *The BCS–BEC Crossover and the Unitary Fermi Gas* (Springer, 2012).
- Törmä, P. & Sengstock, K. *Quantum Gas Experiments: Exploring Many-Body States* (Imperial College Press, 2015).
- Lewenstein, M. et al. Ultracold atomic gases in optical lattices: mimicking condensed matter physics and beyond. *Adv. Phys.* **56**, 243–379 (2007).
- Gross, C. & Bloch, I. Quantum simulations with ultracold atoms in optical lattices. *Science* **357**, 995–1001 (2017).
- Stöferle, T., Moritz, H., Günter, K., Köhl, M. & Esslinger, T. Molecules of fermionic atoms in an optical lattice. *Phys. Rev. Lett.* **96**, 030401 (2006).
- Chin, J. K. et al. Evidence for superfluidity of ultracold fermions in an optical lattice. *Nature* **443**, 961–964 (2006).
- Moritz, H., Stöferle, T., Günter, K., Köhl, M. & Esslinger, T. Confinement induced molecules in a 1D Fermi gas. *Phys. Rev. Lett.* **94**, 210401 (2005).
- Olshanii, M. Atomic scattering in the presence of an external confinement and a gas of impenetrable bosons. *Phys. Rev. Lett.* **81**, 938–941 (1998).
- Bergeman, T., Moore, M. G. & Olshanii, M. Atom–atom scattering under cylindrical harmonic confinement: numerical and analytic studies of the confinement induced resonance. *Phys. Rev. Lett.* **91**, 163201 (2003).
- Venu, V. et al. Observation of unitary  $p$ -wave interactions between fermions in an optical lattice. *Nature* **613**, 262–267 (2023).
- Tokura, Y. & Nagaosa, N. Orbital physics in transition-metal oxides. *Science* **288**, 462–468 (2000).
- Maekawa, S. et al. in *Springer Series in Solid-State Sciences* Vol. 144 (eds Cardona, M. et al.) 1–337 (Springer, 2004).
- Li, X. & Liu, W. V. Physics of higher orbital bands in optical lattices: a review. *Rep. Prog. Phys.* **79**, 116401 (2016).
- Wirth, G., Ölschläger, M. & Hemmerich, A. Evidence for orbital superfluidity in the  $P$ -band of a bipartite optical square lattice. *Nat. Phys.* **7**, 147–153 (2011).
- Kock, T., Hippler, C., Ewerbeck, A. & Hemmerich, A. Orbital optical lattices with bosons. *J. Phys. B* **49**, 042001 (2016).
- Wang, X.-Q. et al. Observation of nematic orbital superfluidity in a triangular optical lattice. Preprint at <https://arxiv.org/abs/2211.05578> (2022).
- Wang, X.-Q. et al. Evidence for an atomic chiral superfluid with topological excitations. *Nature* **596**, 227–231 (2021).
- Hachmann, M., Kiefer, Y. H., Riebesehl, J., Eichberger, R. & Hemmerich, A. Quantum degenerate Fermi gas in an orbital optical lattice. *Phys. Rev. Lett.* **127**, 033201 (2021).
- Chin, C., Grimm, R., Julienne, P. & Tiesinga, E. Feshbach resonances in ultracold gases. *Rev. Mod. Phys.* **82**, 1225–1286 (2010).
- Gribakin, G. F. & Flambaum, V. V. Calculation of the scattering length in atomic collisions using the semiclassical approximation. *Phys. Rev. A* **48**, 546–553 (1993).
- Ticknor, C., Regal, C. A., Jin, D. S. & Bohn, J. L. Multiplet structure of Feshbach resonances in nonzero partial waves. *Phys. Rev. A* **69**, 042712 (2004).
- Falke, S. et al. Potassium ground-state scattering parameters and Born–Oppenheimer potentials from molecular spectroscopy. *Phys. Rev. A* **78**, 012503 (2008).
- Zhang, S. & Ho, T.-L. Atom loss maximum in ultra-cold Fermi gases. *New J. Phys.* **13**, 055003 (2011).
- Petrov, D. S., Salomon, C. & Shlyapnikov, G. V. Diatomic molecules in ultracold Fermi gases—novel composite bosons. *J. Phys. B* **38**, 645–660 (2005).
- Nuske, M. et al. Metastable order protected by destructive many-body interference. *Phys. Rev. Res.* **2**, 043210 (2020).

**Publisher's note** Springer Nature remains neutral with regard to jurisdictional claims in published maps and institutional affiliations.

**Open Access** This article is licensed under a Creative Commons Attribution 4.0 International License, which permits use, sharing, adaptation, distribution and reproduction in any medium or format, as long as you give appropriate credit to the original author(s) and the source, provide a link to the Creative Commons license, and indicate if changes were made. The images or other third party material in this article are included in the article's Creative Commons license, unless indicated otherwise in a credit line to the material. If material is not included in the article's Creative Commons license and your intended use is not permitted by statutory regulation or exceeds the permitted use, you will need to obtain permission directly from the copyright holder. To view a copy of this license, visit <http://creativecommons.org/licenses/by/4.0/>.

© The Author(s) 2023

## Methods

### Mass spectrometry protocol

To uniquely distinguish and selectively count the populations of atoms and Feshbach dimers in the presence of an optical lattice, they are separated in a ballistic time-of-flight protocol, which maps the population of the  $n$ th band to the  $n$ th BZ. This protocol consists of a rapid adiabatic termination of the lattice potential (in 5 ms) followed by a ballistic expansion (in 22 ms). During the second half of the expansion, the magnetic field is tuned to  $B_{\text{img}} = 200.6$  G to enable absorption imaging at the same resonant frequency in each experimental run. For the case that the dimer mass  $M$  is twice that of an atom  $m$ , atoms travel twice as fast compared with homonuclear dimers with the same initial momentum. Hence, this protocol arranges the atoms and dimers in velocity space with a BZ structure scaled up by a factor of 2 for atoms compared with dimers. This is sketched in Extended Data Fig. 1. The figure shows the first and second BZs for atoms in the background (black and orange areas) and for dimers in the foreground (grey and red areas), giving rise to a nested structure of four white squares denoted 1–4. The optical densities integrated across the areas enclosed by these squares are denoted as  $\square_v$ ,  $v \in \{1-4\}$ . We denote the total populations as  $A_v$  and  $D_v$  for atoms and dimers in the band with band index  $v \in \{1, 2\}$ , respectively. If sectors in Extended Data Fig. 1 comprise atoms and dimers, the counting protocol requires the assumption that the first band for atoms is uniformly filled. This assumption is reasonable as, in the experiments described in the main text, we typically start with the lowest band filled with fermionic atoms, form Feshbach dimers, and subsequently excite a fraction of them to the second band without changing their quasi-momenta<sup>24</sup>. Note that due to the bosonic nature of the Feshbach dimers, the respective BZs (red and grey areas in Extended Data Fig. 1) are not necessarily filled homogeneously, as Bose enhancement and hence multiple occupancy of available energy states are possible. Under the condition of a homogeneous filling of the first atomic band, the populations  $A_1$ ,  $A_2$ ,  $D_1$  and  $D_2$  in different sectors of Extended Data Fig. 1 are indicated in the figure accounting for the four-fold rotation symmetry of the BZs and the four times larger BZ areas for atoms. This leads to the following relations:  $A_2 = \square_1 - \square_2$ ,  $A_1 = 2(\square_2 - \square_3)$ ,  $D_2 = \frac{3}{2}\square_3 - \square_4 - \frac{1}{2}\square_2$  and  $D_1 = \frac{1}{2}\square_3 - \frac{1}{2}\square_2 + \square_4$ . If all atoms and dimers reside in the second band, that is,  $A_1 = D_1 = 0$ , the simple case  $A_2 = \square_1 - \square_2$  and  $D_2 = \square_3 - \square_4$  arises, in which case the condition of uniform filling is not required.

### Data availability

All data presented in the figures are available at <https://www.fdr.uni-hamburg.de/record/11240>.

### Code availability

The used numerical codes are based upon Mathematica by Wolfram Inc. and are available upon reasonable request to the corresponding author.

### Acknowledgements

We thank R. Eichberger for help in the early stage of the experiment. We acknowledge support from the Deutsche Forschungsgemeinschaft (DFG) through the collaborative research centre SFB 925 (project no. 170620586, C1). M.H. was partially supported by the Cluster of Excellence CUI: Advanced Imaging of Matter of the Deutsche Forschungsgemeinschaft (DFG)—EXC 2056—project ID 390715994.

### Author contributions

Y.K. and M.H. carried out the experiments and analysed the data with equal contributions. A.H. conceived and supervised the project. All authors discussed the physics and contributed to the writing of the paper.

### Funding

Open access funding provided by Universität Hamburg

### Competing interests

The authors declare no competing interests.

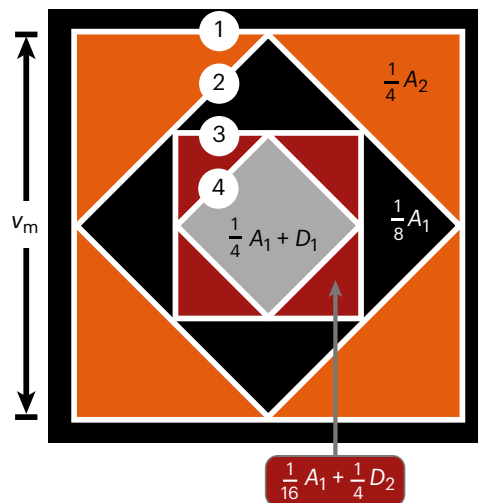
### Additional information

**Extended data** is available for this paper at <https://doi.org/10.1038/s41567-023-01994-9>.

**Correspondence and requests for materials** should be addressed to Andreas Hemmerich.

**Peer review information** *Nature Physics* thanks Stefan Truppe and the other, anonymous, reviewer(s) for their contribution to the peer review of this work.

**Reprints and permissions information** is available at [www.nature.com/reprints](http://www.nature.com/reprints).



**Extended Data Fig. 1 | Evaluation of atom and dimer populations.**  $x$ - $y$  plane of velocity space with  $v_m = \sqrt{2} \hbar k / m$ .  $A_\nu$  and  $D_\mu$  denote the total atom and dimer populations, respectively, within the Bloch bands with band index  $\nu, \mu \in \{1, 2\}$ . The terms  $a_\nu A_\nu + d_\mu D_\mu$ , plotted inside different sectors bordered by white lines, specify the respective total particle numbers.